Diffusion-free Grotthuss topochemistry for high-rate and long-life proton batteries

Xianyong Wu[1], Jessica J. Hong[1], Woochul Shin[1], Lu Ma[2], Tongchao Liu[3], Xuanxuan Bi[3], Yifei Yuan[3], Yitong Qi[1], T. Wesley Surta[1], Wenxi Huang[4], Joerg Neuefeind[5], Tianpin Wu[2], P. Alex Greaney[4]*, Jun Lu[3]* and Xiulei Ji[1]*

The design of Faradaic battery electrodes that exhibit high rate capability and long cycle life equivalent to those of the electrodes of electrical double-layer capacitors is a big challenge. Here we report a strategy to fill this performance gap using the concept of Grotthuss proton conduction, in which proton transfer takes place by means of concerted cleavage and formation of O–H bonds in a hydrogen-bonding network. We show that in a hydrated Prussian blue analogue (Turnbull's blue) the abundant lattice water molecules with a contiguous hydrogen-bonding network facilitate Grotthuss proton conduction during redox reactions. When using it as a battery electrode, we find high-rate behaviours at 4,000 C ($380 A g^{-1}$, $508 mA cm^{-2}$), and a long cycling life of 0.73 million cycles. These results for diffusion-free Grotthuss topochemistry of protons, in contrast to orthodox battery electrochemistry, which requires ion diffusion inside electrodes, indicate a potential direction to revolutionize electrochemical energy storage for high-power applications.

Faradaic electrodes that possess the high capacity of batteries, while simultaneously delivering the high rate capability and excellent cycle life of electrodes in electrical double-layer capacitors, represent a grand challenge for electrochemical energy storage, and a class of such materials would transform our use of electrical energy[1–3]. The rate performance of Faradaic electrodes is partially governed by transportation of ion charge carriers inside electrodes, which in turn depends on the choice of ion charge carriers[4–6]. So far, most attention has been devoted to devices operating on metal ions, starting with Li and looking down the periodic table[7–15]. Relatively little consideration has been given to looking up the periodic table to hydrogen, despite the hydrogen ion—a single proton—being much smaller than any metal ion[16–21]. In addition to its advantage of size, the presence of hydrogen as a constituent of water enables fast conduction of protons in aqueous systems by a displacive mechanism first postulated by von Grotthuss in 1806[22]. In this process, shown in Fig. 1a, an H atom bridging two hydrogen-bonded water molecules switches its allegiance from one molecule to the other, kicking out one of the existing H atoms from its adopted molecule, and triggering a chain of similar displacements through the hydrogen-bonding network[23–25]. The motion is akin to a Newton's cradle (Fig. 1b), with correlated local displacements leading to long-range transport of protons—very different from conduction of metal ions, where solvated metal ions diffuse long distances individually[23–25]. Grotthuss proton conduction is very fast[16,26,27], and it is responsible for the anomalously high conductivity of acids[28]. Recent studies have suggested that Grotthuss conduction may also take place in hydrogen-bonding networks confined inside solids, such as hydrated metal–organic frameworks[29,30]. However, it has thus far remained unknown whether Grotthuss conduction can facilitate the redox reactions in battery electrodes to enable a high rate capability for electrochemical devices.

Herein, we report an electrode material—a defective Prussian blue analogue (PBA), more specifically a Turnbull's blue analogue (TBA), $Cu[Fe(CN)_6]_{0.63}•\square_{0.37}•3.4H_2O$, where $\square$ represents a ferricyanide vacancy; this material explicitly plays out the benefits of Grotthuss proton conduction on the rate and cycling performance of a Faradaic electrode. At the extremely high charging rate of 4,000 C ($380 A g^{-1}$, $508 mA cm^{-2}$), the CuFe-TBA electrode retains half the capacity obtained at 1 C (1 C is defined as $95 mA g^{-1}$)—rivalling the fastest electrodes in any electrochemical storage device. Furthermore, CuFe-TBA maintains 60% of its capacity after 0.73 million cycles at 500 C, the largest number of cycles ever reported for a Faradaic electrode. The CuFe-TBA electrode uses protons as its working ions, providing a fast charge transport mechanism not available to traditional metal–ion batteries. Synchrotron X-ray and neutron diffraction measurements, combined with the first-principles calculations, show that the superlative performance of CuFe-TBA originates from its contiguous network of hydrogen-bonded lattice water, which mediates Grotthuss proton conduction. Taking advantage of Grotthuss topochemistry engenders an exciting avenue for bridging the performance gap between capacitors and batteries.

Crystal structures and electrochemical performance of PBAs

We aim to design electrode materials that harness Grotthuss proton conduction to deliver exceptional power density of batteries. A TBA, $Cu[Fe(CN)_6]_{0.63}•3.4H_2O$ (CuFe-TBA), was selected as a model electrode; it operates in an acidic aqueous electrolyte and has an open framework architecture filled with a crystal water network. TBAs with the specific stoichiometry $M^{II}[Fe^{III}(CN)_6]_{2/3}•\square_{1/3}•4H_2O$ are a subset of the well-known family of PBAs, where M is a transition metal[30,31]. Besides TBA, there are another two classes of PBAs that differ in their vacancies stoichiometry: Berlin

[1]Department of Chemistry, Oregon State University, Corvallis, OR, USA. [2]X-ray Science Division, Advanced Photon Sources, Argonne National Laboratory, Lemont, IL, USA. [3]Chemical Sciences and Engineering Division, Argonne National Laboratory, Lemont, IL, USA. [4]Materials Science and Engineering, University of California, Riverside, CA, USA. [5]Oak Ridge National Laboratory, Oak Ridge, TN, USA. *e-mail: david.ji@oregonstate.edu; junlu@anl.gov; agreaney@engr.ucr.edu
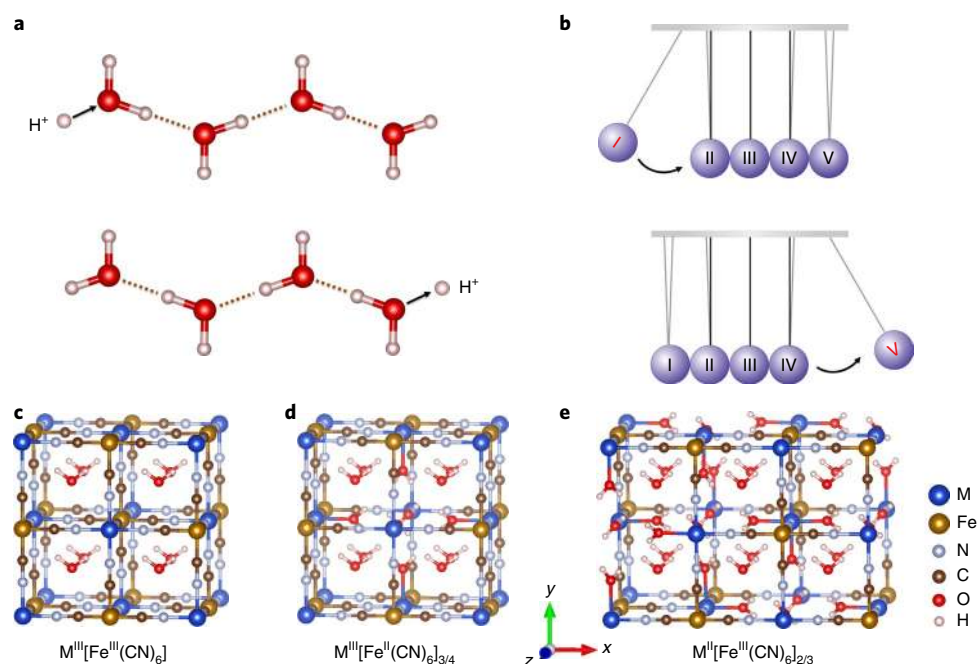
Fig. 1 | Transfer of charges and energy, and three classes of PBAs. a, A schematic of the Grotthuss mechanism, in which proton conduction is operated by rearranging bonds along a water chain. **b**, A schematic of Newton's cradle. **c–e**, Schematic structures of Berlin green, $M^{III}[Fe^{III}(CN)_6]\cdot 2H_2O$ (**c**), IPB, $M^{III}[Fe^{II}(CN)_6]_{3/4}\cdot\square_{1/4}\cdot 3.5H_2O$ (**d**) and Turnbull's blue, $M^{II}[Fe^{III}(CN)_6]_{2/3}\cdot\square_{1/3}\cdot 4H_2O$ (**e**).

green (BG) (also known as Prussian yellow), $M^{III}[Fe^{III}(CN)_6]\cdot 2H_2O$, with no vacancies[32,33], and 'insoluble' Prussian blue (IPB), $M^{III}[Fe^{II}(CN)_6]_{3/4}\cdot\square_{1/4}\cdot 3.5H_2O$, with one-quarter of its ferrocyanide sites vacant (Fig. 1c–e)[34]. In Berlin green, the Fe^{III} and M^{III} are octahedrally coordinated to the carbon and nitrogen ends of the cyanide ions, which creates a cubic framework enclosing interstitial cages containing trapped zeolitic water molecules[32,33]. The cages are closed, isolating the zeolitic water molecules from one another and preventing the formation of a hydrogen-bonded network. In IPB and TBA, however, the charge-compensating ferro- and ferricyanide vacancies open passages between cages. Furthermore, the exposed M ions at each vacancy site are 'passivated' by ligand water molecules[31,34]. The zeolitic water in the cages and the ligand water in the vacancies form a hydrogen-bonding 'sphere' (Fig. 1d,e)[34], and if the vacancies exist on adjacent sites these can connect together to build a percolating hydrogen-bonding network in which Grotthuss topochemistry can occur[19,30].

The large fraction of vacancies in CuFe-TBA and its lattice water network create pathways for Grotthuss conduction that enable the electrode to be charged and discharged to near its theoretical capacity at unprecedented rates, and for hundreds of thousands of cycles. CuFe-TBA was synthesized by aqueous precipitation, and the results of its basic characterization are shown in Supplementary Table 1 and Supplementary Figs. 1–3. Galvanostatic charge/discharge (GCD) measurements of CuFe-TBA in 2.0 M H_2SO_4 electrolyte showed a reversible capacity of 95 mAh g^{-1} (~0.14 mAh cm^{-2}) when discharged at a current rate of 1 C. This capacity corresponds to the storage of 0.91 protons per $Cu[Fe(CN)_6]_{0.63}\cdot 3.4H_2O$ formula unit, thus all the Fe^{III} is reduced to Fe^{II}, and 28% Cu^{II} is converted to Cu^I (refs. [32,35]). We selected CuFe-TBA as the model compound primarily on the basis of its superior cycling stability compared with other MFe-TBA compounds (Supplementary Fig. 4). Additionally, it appears that the 2.0 M H_2SO_4 electrolyte renders the rate performance of CuFe-TBA optimal in comparison with other concentrations (Supplementary Fig. 4).

To study the rate performance of CuFe-TBA, GCD curves recorded at 20 C, 200 C, 2,000 C and 4,000 C show corresponding capacities of 78, 67, 56 and 49 mAh g^{-1}, respectively (Fig. 2a). At 4,000 C, CuFe-TBA discharges in just 0.46 s, but retains half of its 1 C capacity. It is notable in Fig. 2a that the potential hysteresis (polarization) between the charge and discharge profiles increases linearly with the current rate, suggesting that the rate performance of CuFe-TBA is limited more by the testing cells' electrical resistance than the proton transport and the reaction kinetics[32]. Such rate performance is comparable with the fastest electrodes in electrical double-layer capacitors[36,37], and exceeds the high rate performance of most other Faradaic electrodes[20,38–41] (see comparison in Supplementary Fig. 5). The electrochemical performance of CuFe-TBA is robust both to increasing the active mass loading (see Supplementary Fig. 6) and to continued cycling at different current rates (see Supplementary Fig. 7). The outstanding rate performance has made it possible to test CuFe-TBA through 0.73 million cycles at 500 C, over which it retains 60% of its original capacity (Fig. 2b and Supplementary Fig. 7). Despite the nanosized morphology of CuFe-TBA, such high rate performance has never been reported on any PBA compound with metal cations as charge carriers[19,32,33].

To further examine the rate behaviour of CuFe-TBA, cyclic voltammetry curves were recorded at different scan rates, revealing four pairs of redox peaks (Fig. 2c). We attribute the O1/R1 pair at low potentials to Cu^{II}/Cu^I and the remaining peaks at higher potentials to Fe^{III}/Fe^{II}[32,35]. This contrasts with the two-redox-pair behaviour of topochemistry of Na^+, K^+ and NH_4^+ in CuFe-TBA (Supplementary Fig. 8). The results indicate that proton (de)insertion can reveal different chemical environments in CuFe-TBA, particularly the various hydration conditions through hydrogen bonding[19,42–44]. Another distinction between (de)protonation and (de)insertion of Na^+, K^+ or NH_4^+ within CuFe-TBA is the gap between the peak potentials (E_{pa} and E_{pc}) of corresponding anodic and cathodic currents, as shown in Fig. 2c and Supplementary Fig. 8-10. The peak potentials are nearly identical for the pairs R2/O2, R3/O3 and R4/O4
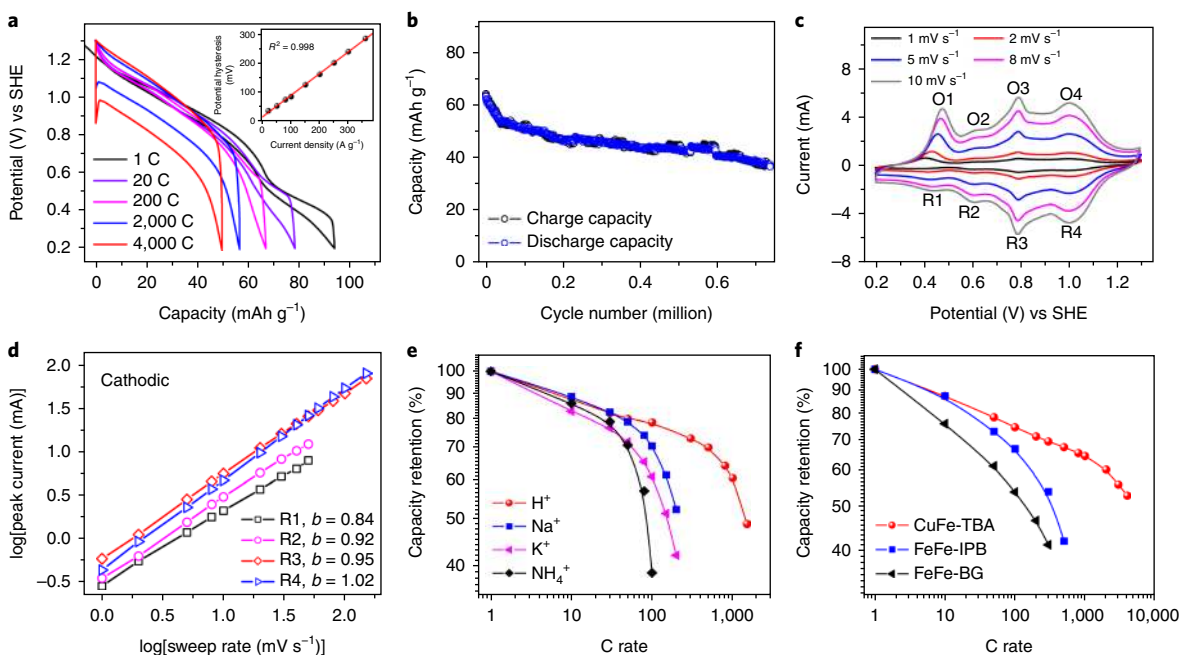
Fig. 2 | Electrochemical performance of CuFe-TBA. a, GCD curves at various current rates. Inset: relationship between the hysteresis of the potential profiles and the applied current rate. The potential is normalized to the SHE. **b**, Cycling performance at 500 C for 0.73 million cycles. **c**, Cyclic voltammetry curves at various scan rates. The O1/R1 peaks correspond to the oxidation and reduction of the Cu^{II}/Cu^{I} redox couple, while the O2/R2, O3/R3 and O4/R4 peaks correspond to the Fe^{III}/Fe^{II} redox couple. **d**, The exponent b values derived from the cyclic voltammetry curves according to the equation $I = av^b$. **e**, The rate performance comparison of CuFe-TBA for different A^+ ions, where the electrolyte is $0.5 \, mol \, l^{-1} \, A_2SO_4$. **f**, The rate performance comparison between CuFe-TBA, FeFe-BG and FeFe-IPB in $2 \, mol \, l^{-1} \, H_2SO_4$ electrolyte.

pertaining to proton storage in CuFe-TBA; however, the gaps of peak potentials within each pair are large for the three metal ions. The aligned cyclic voltammetry peaks are known as characteristics of thin-layer cells or redox reactions of chemisorbed species, where mass diffusion can be neglected[39,45].

The peak current, I, in a cyclic voltammetry curve can be related to the scan rate, v, by the equation $I = av^b$, where a is a coefficient, and in the limiting cases where the kinetics are diffusion controlled or perfectly non-diffusion controlled (capacitive) the exponent b would be either 0.5 or 1.0, respectively[39,45]. The b values for the R4, R3 and R2 peaks are close to unity, indicating strong capacitive behaviour (Fig. 2d). To better demonstrate the advantages in kinetics of the proton (de)insertion inside CuFe-TBA, we also focus on the Fe^{III}/Fe^{II} couple in evaluating the rate capability of CuFe-TBA by adopting a narrower potential range from 0.55 to 1.3 V. At an extremely high current rate of $390 \, A \, g^{-1}$ (6,000 C or $521 \, mA \, cm^{-2}$, where 1 C is defined as $65 \, mA \, g^{-1}$ here), a high capacity utilization of 70% is still attainable (Supplementary Fig. 11). The fast kinetics of redox reactions would not be viable without fast proton conduction within CuFe-TBA. Measurements to verify this found proton conductivity of $3.65 \times 10^{-4} \, S \, cm^{-1}$ at 298 K and 100% humidity give an activation energy (E_a) of 0.28 eV (Supplementary Fig. 12), where an E_a value below 0.4 eV typically suggests Grotthuss conduction[30].

To verify the correlation between the excellent electrochemical performance of CuFe-TBA in the H_2SO_4 electrolyte and the Grotthuss proton conduction mechanism, we used two different approaches to test the rate performance of the material under conditions where Grotthuss topochemistry is non-viable. Grotthuss conduction cannot be active in CuFe-TBA when metal ions are the inserted charge carriers[23-25], and indeed, when storing Na^+, K^+ or NH_4^+ ions, CuFe-TBA delivers poorer rate performance, with b exponents well below unity (Fig. 2e, Supplementary Figs. 13 and 14). A second approach to eliminate Grotthuss conduction is to interrupt the hydrogen-bonding network inside the PBA electrode to

remove contiguous pathways for Grotthuss displacement[30]. IPB and BG have the same framework architecture as CuFe-TBA, but fewer anion vacancies per formula unit and thus poor connectivity of hydrogen bonding between the zeolitic cages. Stochastic models of the vacancy arrangement in IPB (discussed in 'Characterization and simulation of the CuFe-TBA structure') suggest that more than 80% of the hydrogen-bonding network is contiguous. As expected, both BG and IPB exhibit inferior proton (de)insertion kinetics compared with CuFe-TBA in the same acidic aqueous electrolyte (Fig. 2f and Supplementary Fig. 15). These comparative studies highlight the correlation between the Grotthuss mechanism and high rate capability of proton storage in CuFe-TBA.

Characterization and simulation of the CuFe-TBA structure

To understand the structure of the hydrogen-bonding network on which Grotthuss conduction depends, a set of advanced structural characterization experiments was performed in conjunction with density functional theory (DFT) calculations to determine the atomic structure of CuFe-TBA that hosts lattice water. Synchrotron X-ray diffraction (XRD) reveals a typical face-centred cubic structure of the CuFe-TBA framework with a space group of $Fm3\text{-}m$ and a lattice parameter a of 10.12501 Å ($R_{wp} = 4.81\%$, $\chi^2 = 5.45$, R_{wp} and χ^2 reveal the quality of the fitting) (Fig. 3a). Refinement of neutron diffraction patterns from the deuterated samples reveals the presence of three distinguishable water positions of ligand water (O1), centre zeolitic water (O2) and off-centre zeolitic water (O3), respectively (Fig. 3b and Supplementary Fig. 16). Figure 3c depicts the electron density map of a unit cell, where the electron distribution of atoms can be clearly shown. Supplementary Table 2 lists the refined atomic positions and occupancies of CuFe-TBA.

To resolve the water network, DFT calculations were performed to identify the energetically favourable configuration for collections of water molecules confined in the pipework of spaces created by neighbouring ferricyanide vacancies. Calculations were performed
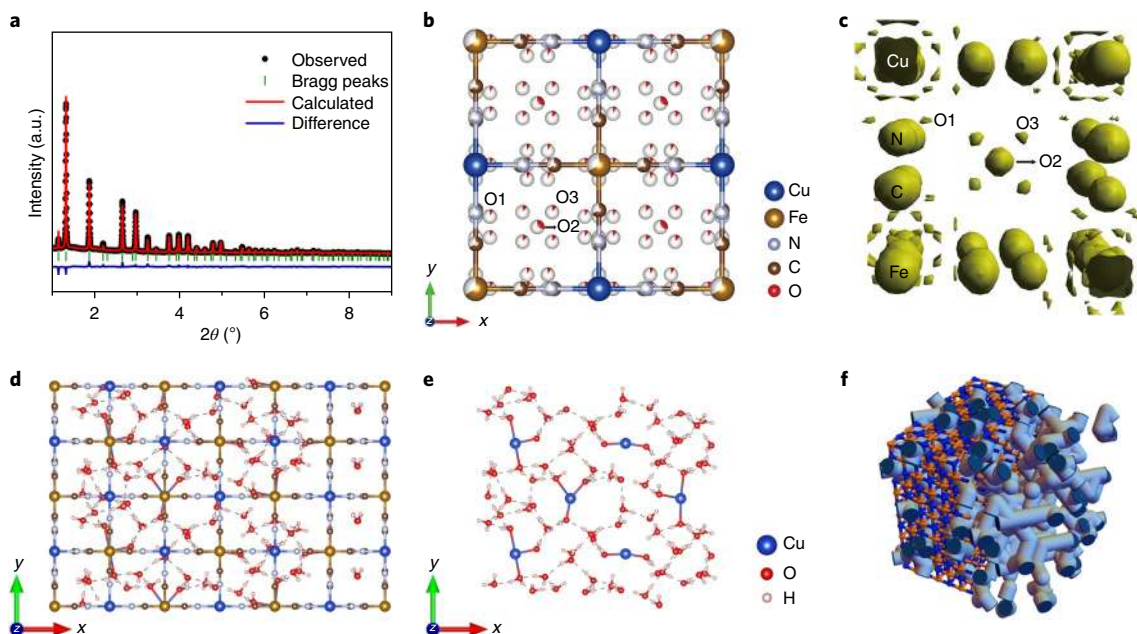
Fig. 3 | Structural studies of CuFe-TBA. a, A synchrotron XRD pattern of CuFe-TBA with the Rietveld refinement. **b**, The refined crystal structure of CuFe-TBA with possible water sites, where red sectors denote the occupancy. **c**, The electron density map of CuFe-TBA's structure. **d**, The DFT calculation of the water orientations in a 3×1×1 supercell of CuFe-TBA. **e**, The orientations and connections of hydrogen-bonded water molecules in **d**, where the framework is omitted for clarity. **f**, A model of a 6×6×6 supercell of CuFe-TBA showing the internal pipework formed by a stochastic configuration of ferricyanide vacancies. Vacancy sites are marked with a blue sphere, and the connections between any adjacent vacancy pairs are marked with blue pipes. The CuFe-TBA framework is not shown in the right half of the figure to better demonstrate the connectivity of the pore network. The system is periodic, and the pipes that have a dark-blue opening are connected to other vacancies across the periodic boundaries. The vacancies were arranged randomly with the constraint that they satisfy local charge neutrality. In the resulting pipework, more than 95% of the vacancies are parts of a percolating pore network.
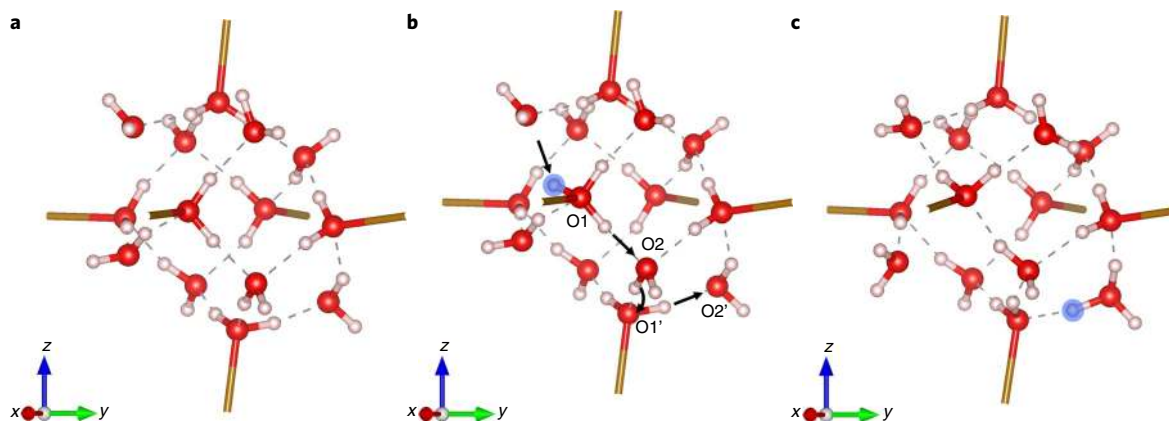
Fig. 4 | DFT calculations of the proton-binding sites. a, Water orientations in the relaxed IPB structure. **b**, A hypothetical ligand hydronium in IPB before relaxation: the introduced proton is highlighted blue, and the arrows represent the proton migration pathway. **c**, Water orientations in the relaxed protonated IPB structure. The IPB framework is omitted here for clarity, but the Cu–O bonds are shown as sticks to differentiate the ligand water (connecting to sticks) from zeolitic water.

using a 3×1×1 supercell of the face-centred cubic lattice, which is the smallest volume that possesses the CuFe-TBA 3:2:12 stoichiometry of Cu:Fe:H$_2$O (Supplementary Fig. 17). As shown in Fig. 3d,e and Supplementary Fig. 18, after relaxation, both ligand and zeolitic water molecules cooperatively form a hydrogen-bonding network. Moreover, when CuFe-TBA is soaked in the electrolyte, it will absorb additional water into its zeolitic cages, and thus contain more lattice water than the dry samples characterized by diffraction[30,31]. Therefore, the hydrogen-bonding network can only be more populous and denser than the simulated network. The DFT

calculations show the connectivity of the water network within the pipe formed by two adjacent vacancies, but long-range transport also requires the vacancies to be arranged so that the pipework is percolating. Figure 3f and Supplementary Fig. 19 show the stochastic models of the vacancy pipework in 6×6×6 supercells of IPB and TBA. Whereas in IPB there are 25 pipe sets and more than 80% of the pipework is percolating, in the TBA the pipework is considerably less tortuous, with just two percolating pipe systems accounting for more than 95% of the porosity. Taken together, the characterization and simulation results clearly support the
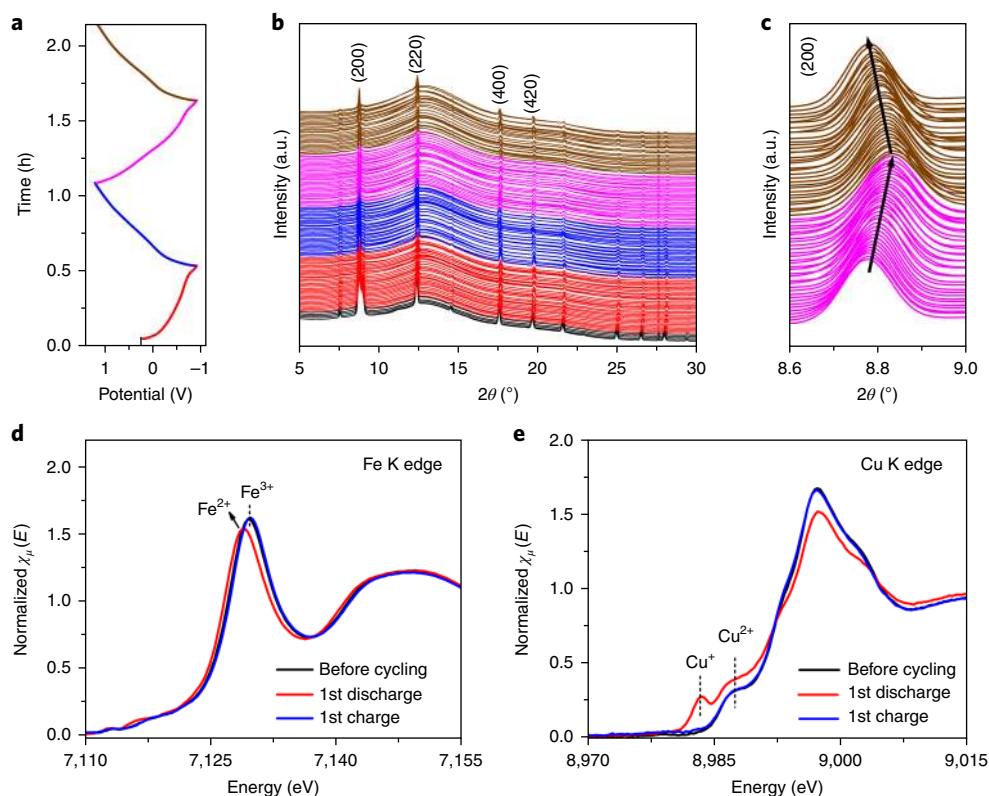
Fig. 5 | Structural evolution during proton (de)insertion. a, GCD profiles of the CuFe-TBA||activated carbon coin cells. **b**, Operando synchrotron XRD patterns of the CuFe-TBA electrode. **c**, An enlarged view of the (200) peak from the XRD patterns in **b**. The black, red, blue, magenta and brown colours represent the initial cell resting, the first discharge, the first charge, the second discharge and the second charge, respectively. **d**, In situ XANES of the Fe K-edge spectra. **e**, XANES of the Cu K edge. $\chi_\mu(E)$ represents the absorption coefficient in the spectra.

correlation between the Grotthuss mechanism and the high rate capability of CuFe-TBA.

Proton-binding sites and conduction activation energy

The protons inserted in CuFe-TBA will bind with lattice water molecules to form hydronium—H_3O^+ (refs. [24–27]). Therefore, it is critical to understand whether zeolitic or ligand water is the more favourable binding site. We employed the DFT calculations to compare the energetics of proton binding on the two sites. To save computation expense, we selected the IPB structure as the model, as it is the smallest unit cell that hosts two types of lattice water. We simulated several possible water orientations in the neutral IPB structure and chose the geometry with the lowest energy as the starting compound, as shown in Fig. 4a and Supplementary Fig. 20. We first modelled the protonated IPB that contains a ligand hydronium, where the inserted proton is highlighted in blue (Fig. 4b). For better visualization, the IPB framework is omitted and only the water molecules are shown. Interestingly, after relaxation, this proton migrates to a zeolitic water site, as displayed in Fig. 4c and Supplementary Fig. 21, which suggests a lower energy of the zeolitic water site for proton binding. To further verify this, we also computed a protonated IPB with a zeolitic hydronium, which, after relaxation, still retains the zeolitic hydronium configuration besides some subtle orientation adjustments (Supplementary Fig. 22). The results suggest that zeolitic water is energetically more favourable for proton binding. This can be rationalized by the fact that the oxygen atom of the ligand water is strongly bound to the transition metal cations, which discourages the formation of the ligand hydronium. A similar phenomenon has been reported by previous studies: a hydronium cation prevents other cations from coordinating with its oxygen[24,25].

On the other hand, the relaxation calculations support the concept of Grotthuss conduction of protons inside the CuFe-TBA structure. As shown by Supplementary Video 1, the proton 'migrates' along a water chain via cooperative cleavage and reconnection of the covalent and hydrogen bonds, that is, from the ligand water O1, a starting point, to the nearby zeolitic water O2, then to the next ligand water O1', and finally to zeolitic water O2'. Such migration clearly has little to do with the vehicle mechanism. The relaxation showcases a journey of a proton driven by energetics to reach its most stable state, resembling a chemical process that works its way to the 'equilibrium' state. Such relaxation can, thus, simulate the local ion–electrode interaction for processes where the equilibrium state is defined by an applied potential, for example, during electrochemical potentiostatic titration tests.

To further verify our hypothesis, we calculated the energy barrier of proton hopping from a zeolitic water to the neighbouring ligand water site. As shown in Supplementary Figs. 23 and 24, the initial proton hopping and the subsequent water cluster reorientation constitute the entire activation process, where a very low energy barrier of 0.15 eV (<0.4 eV) unambiguously indicates Grotthuss conduction[23–30].

The computation results, including the percolation of the lattice water network inside CuFe-TBA, the proton migration process during relaxation and the calculated activation energy barrier, collectively suggest that the proton migration in the TBA structure is Grotthuss conduction, which rationalizes the extremely high-rate proton (de)insertion. However, we should note that the effect of fast proton conduction in electrochemical reactions can be masked by the kinetics of redox reactions as the driving force of proton conduction as well as electronic resistance of testing cells.

Structural evolution during proton (de)insertion

To better understand the superior cycling performance of CuFe-TBA, we carried out operando synchrotron XRD to investigate the structural change of the CuFe-TBA host framework during the proton topochemistry. As shown in Fig. 5b, CuFe-TBA maintains its face-centred cubic structure during the entire proton insertion and de-insertion processes. Close examination of the (200) peak reveals that CuFe-TBA undergoes slight lattice shrinkage during proton insertion and reversible lattice expansion on proton de-insertion, as shown in Fig. 5c, which is primarily due to the smaller radius of the $[Fe(CN)_6]^{4-}$ than $[Fe(CN)_6]^{3-}$ anions[32,33]. The lattice shrinkage from 10.12 to 10.05 Å during the proton insertion corresponds to a low volume change of 2%; this minimal volume change may be responsible for the exceptional cycling stability.

To confirm the changes of oxidation states of Cu and Fe elements during proton insertion/de-insertion, we conducted in situ X-ray adsorption near edge spectroscopy (XANES) measurements. As shown in Fig. 5d,e, after proton insertion, the Fe K-edge XANES exhibits a peak shift from 7,129.6 to 7,128.8 eV, suggesting the reduction of Fe^{III} to Fe^{II}, and a new peak of the Cu K-edge XANES emerges at 8,983.4 eV, indicating partial reduction of Cu^{II} cations. When protons are de-inserted, both Fe and Cu K-edge spectra are restored to their original positions, demonstrating a reversible valence state change. Interestingly, the redox transition of the Cu^{II}/Cu^{I} couple in CuFe-TBA is more pronounced when storing protons than their metal counterparts Na^+ and K^+ (Supplementary Fig. 8), which gives rise to a higher capacity for proton storage. It is likely that the much smaller proton manages to probe more redox-active sites in the CuFe-TBA structure, which activates the Cu^{II}/Cu^{I} redox chemistry. Overall, the CuFe-TBA cathode exhibits a higher capacity, much better rate performance and excellent cycling stability for proton topochemistry.

To further demonstrate the concept of proton batteries, we coupled the chemically reduced CuFe-TBA as a cathode with a WO_3 anode, which gives rise to a promising proton battery fuel cell with an average voltage of about 1.0 V. The full cell also demonstrated promising cycling performance, where after 1,000 cycles the capacity fades from 50 to 37 mAh g^{-1} (based on the mass of the CuFe-TBA cathode), corresponding to a capacity retention of about 74% (Supplementary Fig. 25).

Conclusions

In summary, we have discovered that Grotthuss topochemistry leads to extremely high rate performance and extraordinarily long cycle life of CuFe-TBA as a proton battery electrode. The discovery offers a feasible approach for storage batteries based on Grotthuss topochemistry in which CuFe-TBA is just one example of a plethora of hydrated solid structures that could serve as electrodes for high-power proton batteries. This study has explored to some extent the fundamental limits of high-current topotactic battery chemistry, and while the results are exciting, this is about the theoretical potential of a new technology. Tremendous challenges must still be overcome to realize ultrafast charge and discharge in practical batteries for transportation or grid energy storage. Systems operating on other charge carriers may also exhibit Grotthuss-like conduction in battery electrodes, where such carriers may be OH^-/H_2O or I_2/I^- (refs. [46,47]), which warrants further investigation.

Methods

Material preparation. The TBA—$Cu^{II}[Fe^{III}(CN)_6]_{2/3}$•$4H_2O$ (denoted as CuFe-TBA)—was prepared by an aqueous precipitation method[31]. Typically, 40 ml of $CuSO_4$ solution (0.2 M) was added dropwise into 40 ml of $K_3Fe(CN)_6$ solution (0.1 M) under magnetic stirring. After 6 h of reaction, the olive-green precipitate was rinsed with deionized water and centrifuged multiple times, and then dried in an oven at 60 °C overnight. The deuterated CuFe-TBA samples for neutron studies were prepared in a N_2-filled glovebox, and we used deuterated water as the reaction medium. The precipitates were rinsed with deuterated water several times and dried in a N_2-filled oven at 60 °C overnight.

The Berlin green sample, $Fe^{III}[Fe^{III}(CN)_6]$•$2H_2O$ (denoted as FeFe-BG), was prepared by an acid-assisted precipitation method[48]. Typically, 80 ml of $K_3Fe(CN)_6$ solution (0.1 M) was first acidified by hydrochloric acid to pH 1, and then heated to 80 °C with continuous stirring. After 12 h of reaction, the dark-green precipitate was rinsed with deionized water and centrifuged multiple times, and then dried in a 60 °C oven overnight.

The IPB sample, $Fe^{III}[Fe^{II}(CN)_6]_{3/4}$•$3.5H_2O$ (denoted as FeFe-IPB), was prepared by an aqueous precipitation reaction[34]. Typically, 40 ml of $FeCl_3$ solution (0.15 M) was added dropwise into 40 ml of $K_4Fe(CN)_6$ solution (0.10 M) under stirring. After 6 h of reaction, the dark-blue precipitate was rinsed with deionized water and centrifuged multiple times, and then dried in a 60 °C oven overnight.

Material characterization. The general chemical compositions of PBAs are usually expressed as $A_xM[Fe(CN)_6]_y$•$\square_{1-y}$•zH_2O, where A represents alkali metal[34,49]. We utilized inductively coupled plasma optical emission spectrometry (Perkin Elmer 2100 DV) to calibrate K, M and Fe ions, elemental analysis (Elementar Vario Macro Cube) to analyse C and N elements, and thermogravimetric analysis (SDTQ600, TA Instruments) to determine water content. Thus, the chemical compositions of the CuFe-TBA, FeFe-BG and FeFe-IPB were determined as $Cu[Fe(CN)_6]_{0.63}$•$\square_{0.37}$•$3.4H_2O$, $Fe[Fe(CN)_6]_{0.94}$•$\square_{0.06}$•$1.6H_2O$ and $Fe[Fe(CN)_6]_{0.73}$•$\square_{0.27}$•$3.5H_2O$, respectively. Transmission electron microscopy images of PBAs were observed on a JEOL-2010 microscope. Ex situ synchrotron XRD patterns of CuFe-TBA were collected on the 11-ID-C beamline of the Advanced Photon Source (APS), Argonne National Laboratory, where the wavelength was 0.1173 Å. XANES spectra of the Fe edge and Cu edge for CuFe-TBA samples were collected at APS on beamline 9-BM-B with an electron energy of 7 GeV and average current of 100 mA in transmission mode. The radiation was monochromatized by a Si(111) double-crystal monochromator. Harmonic rejection was accomplished with a harmonic rejection mirror. For energy calibration, the peak position of the first derivative of Co foil was adjusted to 7709 eV. XANES data reduction and analysis were processed by Athena software. For operando synchrotron XRD characterization of CuFe-TBA electrodes, powder XRD patterns were collected at experimental station 13-BM-C of APS. The X-ray beam was monochromated by a Si(311) crystal to 28.6 keV (0.434 Å) with 1 eV bandwidth. A Kirkpatrick–Baez mirror system was used to obtain a vertical×horizontal focus spot size of 20 μm × 30 μm, measured as full width at half maximum. The diffraction pattern was collected in transmission mode, and an MAR165 CCD (charge coupled device) detector (Rayonix) was placed about 180 mm away from the sample. The typical exposure time was 60 s for each diffraction pattern. The neutron diffraction on the deuterated CuFe-TBA was conducted at the Nanoscale Ordered Materials Diffractometer, Spallation Neutron Source, Oak Ridge National Laboratory. Samples were loaded into quartz capillaries for analysis.

Electrochemical tests. To prepare the working electrodes, 70 wt% PBA, 20 wt% Ketjen black carbon and 10 wt% polyvinylidene fluoride binder were first ground in a mortar to form a homogeneous slurry. The slurry was cast onto carbon fibre paper (Fuel Cells Etc, 381 μm in thickness and 1.0 cm in diameter) as the current collector[18,32,33], and allowed to dry in an oven at 60 °C. The active mass loading for PBAs is about 1.5 mg cm^{-2}. For higher active mass loadings of 7 and 9 mg cm^{-2}, we fixed the mass ratio between CuFe-TBA and Ketjen black carbon to 7:2 but increased the mass of polyvinylidene fluoride binder. As a result, the mass ratio is 58.3 wt% CuFe-TBA, 16.7 wt% Ketjen black and 25.0 wt% polyvinylidene fluoride. The areal capacities of the CuFe-TBA electrodes are thus calculated as about 0.14, 0.29, 0.67 and 0.86 mAh cm^{-2} for mass loadings of about 1.5, 3.0, 7.0 and 9.0 mg cm^{-2}, respectively. The counter electrode is a free-standing activated carbon film, which is composed of 70 wt.% activated carbon, 20 wt.% Ketjen black carbon, and 10 wt.% polytetrafluoroethylene binder, and the mass loading of activated carbon is 30-50 mg cm^{-2}.

The electrochemical performance of PBAs was characterized in three-electrode Swagelok cells, in which a PBA electrode, an activated carbon film and an Ag/AgCl electrode serve as the working electrode, counter-electrode and reference electrode, respectively. The separator was Whatman filter paper, and the electrolytes were 2.0 M H_2SO_4 or 0.5 M A_2SO_4 (A = H^+, Na^+, K^+ and NH_4^+) aqueous solutions. When compared with other acid electrolytes such as CH_3COOH, H_3PO_4 and HCl, H_2SO_4 exhibits good ionic conductivity and a large electrochemical stability window, and was thus selected as the electrolyte for proton (de)insertion (Supplementary Fig. 26). The cell was assembled in a N_2-filled glovebox, and the electrolyte was purged with N_2 gas for 30 min before use. Note that for electrochemical tests on H^+, Na^+ and NH_4^+ ions we replaced the saturated KCl solution in the reference electrode with HCl, NaCl or NH_4Cl solution, respectively, of the same concentration of about 4.5 M, to prevent possible contamination of the K ions from the reference electrode. After replacement of the supporting electrolyte, the potentials of these reference electrodes were calibrated against the standard reference electrode accordingly. We transferred the reaction potentials from Ag/AgCl to the standard hydrogen electrode (SHE). As for operando synchrotron XRD and in situ XANES characterization, we made coin cells that contained CuFe-TBA as the working electrode and an activated carbon film as both the counter- and reference electrodes. To facilitate X-ray transmission, the coin cell was designed to have a hole in the battery cap but was sealed by a Kapton tape. The potential range for such coin cells was determined from three-electrode cells, which recorded the potential differences

of CuFe-TBA versus the activated carbon electrode as well as versus the reference electrode. To evaluate the self-discharge, after being charged to 1.3 V versus SHE, the CuFe-TBA electrode rested at open circuit voltage for 24 h, and then discharged to 0.2 V (Supplementary Fig. 27). The robust structure and low solubility of CuFe-TBA not only give rise to an excellent cycling performance, but also rule out the possibility of the formation of toxic HCN gas in the acidic solution[32].

The cyclic voltammetry, GCD and rate performance of PBAs were recorded on a VMP-3 multichannel workstation (Bio-Logic Science Instruments), which has a resolution of 5 μV, an acquisition time of 20 μs and a maximum output current of 400 mA. For rate tests, the potential hysteresis in GCD is defined as the voltage gap between the charge and discharge at 50% state of charge. The cycling performance of CuFe-TBA was tested on an Arbin BT2000 system at room temperature.

Proton conductivity tests. The CuFe-TBA powder was first compressed into a pellet with a diameter of 10 mm and a thickness of 0.5 mm. Then the pellet was assembled into a coin cell, in which a wet cotton ball was placed to maintain the 100% humidity during tests. Electrochemical impedance spectroscopy tests were recorded on a VMP-3 multichannel workstation, where the oscillation amplitude is 20 mV and the frequencies range from 1 MHz to 0.1 Hz. The proton conductivity was determined by equation (1)[30,48]:

$$\sigma = L/R_b S \tag{1}$$

where σ, L, S and R_b represent the proton conductivity, thickness of pellet, contact area and bulk resistance, respectively.

We conducted electrochemical impedance spectroscopy tests at different temperatures and calculated the corresponding proton conductivities. E_a can be determined according to the following equation[30,50]:

$$\ln(\sigma T) = \ln A - E_a/k_B T \tag{2}$$

where T, A, k_B and E_a represents the temperature, pre-exponential factor, Boltzmann constant and activation energy for proton conduction, respectively.

Theoretical calculations. The Vienna ab initio Simulation Package (VASP)[51,52] was implemented under the projector augmented wave pseudopotentials[53] with the generalized gradient approximation of the Perdew–Burke–Ernzerhof[54] exchange–correlation function. An energy cut-off of 550 eV with a Monkhorst–Pack[55] reciprocal space grid of a $1 \times 1 \times 1$ k-point scheme was used for the supercell structure. Atomic coordinates were fully relaxed until the forces of each atom were below 0.01 eV Å^{-1}. The supercell of CuFe-TBA was made up of a $3 \times 1 \times 1$ cell, which has a specific stoichiometry of Cu/Fe/H$_2$O = 3/2/12 and can be thus considered as the unit cell. Note that we attached $3 \times 1 \times 0.5$ layers on the top and at the bottom of the $3 \times 1 \times 1$ structure, respectively, to better show the water orientations in the relaxed structure. In order to describe the on-site Coulombic interaction, the DFT + U method[56] was used, where U values were adopted from previously benchmarked literature[57].

To simulate the stochastic models of the vacancy pipework, we generated the $6 \times 6 \times 6$ supercells of IPB and TBA using MATLAB (Mathworks, MATLAB R2015b). According to the chemical stoichiometry of Cu[Fe(CN)$_6$]$_{2/3}$•$_{□1/3}$ and Fe[Fe(CN)$_6$]$_{3/4}$•$_{□1/4}$, the supercells contain 288 and 216 Fe(CN)$_6$ vacancies, respectively, and these vacancies are randomly distributed in the initial state. We calculated the potential energy of these supercells in Large-scale Atomic/Molecular Massively Parallel Simulator and applied the Metropolis Monte Carlo method to reorganize the distribution of vacancies[58,59]. The Metropolis Monte Carlo method is an iterative loop, where in each step a random combination of a vacancy and an anion cluster is chosen to switch positions to form a new state, and if the potential energy of the new state is lower, with a possibility of $p < \exp\left(-\frac{\Delta E}{k_B T}\right)$ the loop accepts this change and starts the next step; if the potential energy is higher, we roll the 'dice' again[59]. After repeating the loop enough times (~30,000 steps), we selected the most stable vacancy arrangement with the lowest potential energy. In the final-state structure, some vacancies are connected as the pipework, which facilitates the cooperative connection of ligand and zeolitic water molecules to constitute a hydrogen-bonding network.

To better visualize the proton migration paths in the PBA's structure during relaxation, we exported the coordinate data after each ionic relaxation step. The freeware visualization tool OVITO was used to make the video[60], and we scaled down the 'sizes' of Fe, C, and N atoms for clarity of the proton conduction through the hydrogen bond rearrangement. To calculate the energy barrier for proton conduction, we performed nudged elastic band simulations[61,62]. The minimum energy pathway via Grotthuss conduction was monitored by forming at least four transition states between the donating and accepting water molecules, followed by obtaining the total energy at each stage. In the NEB calculation, the energy cutoff was 750 eV to expand the electronic wavefunction, and $1 \times 1 \times 1$ Monkhorst–Pack k-point meshes were used.

Data availability

The additional data related to this study are available from the corresponding authors upon request.

References

1. Armand, M. & Tarascon, J. M. Building better batteries. *Nature* **451**, 652–657 (2008).
2. Dunn, B., Kamath, H. & Tarascon, J.-M. Electrical energy storage for the grid: a battery of choices. *Science* **334**, 928–935 (2011).
3. Simon, P., Gogotsi, Y. & Dunn, B. Where do batteries end and supercapacitors begin? *Science* **343**, 1210–1211 (2014).
4. Yang, Z. et al. Electrochemical energy storage for green grid. *Chem. Rev.* **111**, 3577–3613 (2011).
5. Kang, B. & Ceder, G. Battery materials for ultrafast charging and discharging. *Nature* **458**, 190–193 (2009).
6. Evanko, B. et al. Efficient charge storage in dual-redox electrochemical capacitors through reversible counterion-induced solid complexation. *J. Am. Chem. Soc.* **138**, 9373–9376 (2016).
7. Goodenough, J. B. & Park, K.-S. The Li-ion rechargeable battery: a perspective. *J. Am. Chem. Soc.* **135**, 1167–1176 (2013).
8. Li, W., Dahn, J. R. & Wainwright, D. S. Rechargeable lithium batteries with aqueous electrolytes. *Science* **264**, 1115–1117 (1994).
9. Luo, J.-Y., Cui, W.-J., He, P. & Xia, Y.-Y. Raising the cycling stability of aqueous lithium-ion batteries by eliminating oxygen in the electrolyte. *Nat. Chem.* **2**, 760–765 (2010).
10. Suo, L. et al. "Water-in-salt" electrolyte enables high-voltage aqueous lithium-ion chemistries. *Science* **350**, 938–943 (2015).
11. Yabuuchi, N., Kubota, K., Dahbi, M. & Komaba, S. Research development on sodium-ion batteries. *Chem. Rev.* **114**, 11636–11682 (2014).
12. Komaba, S., Hasegawa, T., Dahbi, M. & Kubota, K. Potassium intercalation into graphite to realize high-voltage/high-power potassium-ion batteries and potassium-ion capacitors. *Electrochem. Commun.* **60**, 172–175 (2015).
13. Aurbach, D. et al. Prototype systems for rechargeable magnesium batteries. *Nature* **407**, 724–727 (2000).
14. Lin, M.-C. et al. An ultrafast rechargeable aluminium-ion battery. *Nature* **520**, 324–328 (2015).
15. Kundu, D., Adams, B. D., Duffort, V., Vajargah, S. H. & Nazar, L. F. A high-capacity and long-life aqueous rechargeable zinc battery using a metal oxide intercalation cathode. *Nat. Energy* **1**, 16119 (2016).
16. Ardizzone, S., Fregonara, G. & Trasatti, S. "Inner" and "outer" active surface of RuO$_2$ electrodes. *Electrochim. Acta* **35**, 263–267 (1990).
17. Emanuelsson, R., Sterby, M., Strømme, M. & Sjödin, M. An all-organic proton battery. *J. Am. Chem. Soc.* **139**, 4828–4834 (2017).
18. Sun, W. et al. Zn/MnO$_2$ battery chemistry with H$^+$ and Zn^{2+} coinsertion. *J. Am. Chem. Soc.* **139**, 9775–9778 (2017).
19. Lee, J. H., Ali, G., Kim, D. H. & Chung, K. Y. Metal–organic framework cathodes based on a vanadium hexacyanoferrate Prussian blue analogue for high-performance aqueous rechargeable batteries. *Adv. Energy Mater.* **7**, 1601491 (2017).
20. Lukatskaya, M. R. et al. Ultra-high-rate pseudocapacitive energy storage in two-dimensional transition metal carbides. *Nat. Energy* **2**, 17105 (2017).
21. Carlson, C. E. The proton radius puzzle. *Prog. Part. Nucl. Phys.* **82**, 59–77 (2015).
22. Grotthuss, C. J. T. Sur la decomposition de l'eau et des corps q'uelle tient en dissolution à l'aide de l'électricité galvanique. *Ann. Chim.* **LVIII**, 54–74 (1806).
23. Wolke, C. T. et al. Spectroscopic snapshots of the proton-transfer mechanism in water. *Science* **354**, 1131–1135 (2016).
24. Knight, C. & Voth, G. A. The curious case of the hydrated proton. *Acc. Chem. Res.* **45**, 101–109 (2011).
25. Agmon, N. The Grotthuss mechanism. *Chem. Phys. Lett.* **244**, 456–462 (1995).
26. Thämer, M., De Marco, L., Ramasesha, K., Mandal, A. & Tokmakoff, A. Ultrafast 2D IR spectroscopy of the excess proton in liquid water. *Science* **350**, 78–82 (2015).
27. Marx, D., Tuckerman, M. E., Hutter, J. & Parrinello, M. The nature of the hydrated excess proton in water. *Nature* **397**, 601–604 (1999).
28. Gileadi, E. & Kirowa-Eisner, E. Electrolytic conductivity—the hopping mechanism of the proton and beyond. *Electrochim. Acta* **51**, 6003–6011 (2006).
29. Shimizu, G. K., Taylor, J. M. & Kim, S. Proton conduction with metal–organic frameworks. *Science* **341**, 354–355 (2013).
30. Ohkoshi, S.-i et al. High proton conductivity in Prussian blue analogues and the interference effect by magnetic ordering. *J. Am. Chem. Soc.* **132**, 6620–6621 (2010).
31. Kaye, S. S. & Long, J. R. Hydrogen storage in the dehydrated Prussian blue analogues M$_3$[Co(CN)$_6$]$_2$ (M = Mn, Fe, Co, Ni, Cu, Zn). *J. Am. Chem. Soc.* **127**, 6506–6507 (2005).
32. Wessells, C. D., Huggins, R. A. & Cui, Y. Copper hexacyanoferrate battery electrodes with long cycle life and high power. *Nat. Commun.* **2**, 550 (2011).

33. Wessells, C. D., Peddada, S. V., Huggins, R. A. & Cui, Y. Nickel hexacyanoferrate nanoparticle electrodes for aqueous sodium and potassium ion batteries. *Nano Lett.* **11**, 5421–5425 (2011).

34. Herren, F., Fischer, P., Ludi, A. & Hälg, W. Neutron diffraction study of Prussian blue, $Fe_4[Fe(CN)_6]_3 \cdot xH_2O$. Location of water molecules and long-range magnetic order. *Inorg. Chem.* **19**, 956–959 (1980).

35. Asakura, D. et al. Bimetallic cyanide-bridged coordination polymers as lithium ion cathode materials: core@shell nanoparticles with enhanced cyclability. *J. Am. Chem. Soc.* **135**, 2793–2799 (2013).

36. Sun, H. et al. Three-dimensional holey-graphene/niobia composite architectures for ultrahigh-rate energy storage. *Science* **356**, 599–604 (2017).

37. Liu, C., Li, F., Ma, L. P. & Cheng, H. M. Advanced materials for energy storage. *Adv. Mater.* **22**, 28–62 (2010).

38. Zhang, H., Yu, X. & Braun, P. V. Three-dimensional bicontinuous ultrafast-charge and -discharge bulk battery electrodes. *Nat. Nanotech.* **6**, 277–281 (2011).

39. Augustyn, V. et al. High-rate electrochemical energy storage through Li^+ intercalation pseudocapacitance. *Nat. Mater.* **12**, 518–522 (2013).

40. Zheng, J. et al. Janus solid–liquid interface enabling ultrahigh charging and discharging rate for advanced Lithium-ion batteries. *Nano. Lett.* **15**, 6102–6109 (2015).

41. Lee, S. W. et al. High-power lithium batteries from functionalized carbon-nanotube electrodes. *Nat. Nanotech.* **5**, 531–537 (2010).

42. Augustyn, V. & Gogotsi, Y. 2D materials with nanoconfined fluids for electrochemical energy storage. *Joule* **1**, 443–452 (2017).

43. Zwier, T. S. The structure of protonated water clusters. *Science* **304**, 1119–1120 (2004).

44. Wei, M. et al. A large protonated water cluster $H^+(H_2O)_{27}$ in a 3D metal–organic framework. *J. Am. Chem. Soc.* **128**, 13318–13319 (2006).

45. Wang, J., Polleux, J., Lim, J. & Dunn, B. Pseudocapacitive contributions to electrochemical energy storage in TiO_2 (anatase) nanoparticles. *J. Phys. Chem. C* **111**, 14925–14931 (2007).

46. Tuckerman, M. E., Marx, D. & Parrinello, M. The nature and transport mechanism of hydrated hydroxide ions in aqueous solution. *Nature* **417**, 925–929 (2002).

47. Bai, Y. et al. High-performance dye-sensitized solar cells based on solvent-free electrolytes produced from eutectic melts. *Nat. Mater.* **7**, 626–630 (2008).

48. Wu, X. et al. Low defect $FeFe(CN)_6$ framework as stable host material for high performance Li-ion batteries. *ACS Appl. Mater. Interfaces* **8**, 23706–23712 (2016).

49. Asakura, D. et al. Fabrication of a cyanide-bridged coordination polymer electrode for enhanced electrochemical ion storage ability. *J. Phys. Chem. C* **116**, 8364–8369 (2012).

50. Ono, K. et al. Grain-boundary-free super-proton conduction of a solution-processed Prussian-blue nanoparticle film. *Angew. Chem. Int. Ed.* **56**, 5531–5535 (2017).

51. Kresse, G. & Hafner, J. Ab initio molecular dynamics for liquid metals. *Phys. Rev. B* **47**, 558 (1993).

52. Kresse, G. & Hafner, J. Ab initio molecular-dynamics simulation of the liquid-metal-amorphous-semiconductor transition in germanium. *Phys. Rev. B* **49**, 14251 (1994).

53. Blöchl, P. E. Projector augmented-wave method. *Phys. Rev. B* **50**, 17953 (1994).

54. Perdew, J. P., Burke, K. & Ernzerhof, M. Generalized gradient approximation made simple. *Phys. Rev. Lett.* **77**, 3865–3868 (1996).

55. Monkhorst, H. J. & Pack, J. D. Special points for Brillouin-zone integrations. *Phys. Rev. B* **13**, 5188 (1976).

56. Dudarev, S., Botton, G., Savrasov, S., Humphreys, C. & Sutton, A. Electron-energy-loss spectra and the structural stability of nickel oxide: an LSDA + U study. *Phys. Rev. B* **57**, 1505 (1998).

57. Ling, C., Chen, J. & Mizuno, F. First-principles study of alkali and alkaline earth ion intercalation in iron hexacyanoferrate: the important role of ionic radius. *J. Phys. Chem. C* **117**, 21158–21165 (2013).

58. Plimpton, S. Fast parallel algorithms for short-range molecular dynamics. *J. Comput. Phys.* **117**, 1–19 (1995).

59. Robert, C. P. *Casella Monte Carlo Statistical Methods* 2nd edn (Springer, New York, 2004).

60. Stukowski, A. Visualization and analysis of atomistic simulation data with OVITO—the Open Visualization Tool. *Model. Simul. Mater. Sci. Eng.* **18**, 015012 (2010).

61. Henkelman, G., Uberuaga, B. & Jonsson, H. A climbing image nudged elastic band method for finding saddle points and minimum energy paths. *J. Chem. Phys.* **113**, 9901–9904 (2000).

62. Henkelman, G. & Jonsson, H. Improved tangent estimate in the nudged elastic band method for finding minimum energy paths and saddle points. *J. Chem. Phys.* **113**, 9978–9985 (2000).

Author contributions

X.J. conceived the idea and designed the research. X.W. conducted the material preparation, electrochemical tests and data analyses with assistance from Y.Q. J.J.H. and T.W.S. performed Rietveld refinements of the synchrotron X-ray and neutron diffraction results. P.A.G. supervised the DFT calculations that W.S. and W.H. carried out. J.L. and T.W. supervised the synchrotron-based characterization and transmission electron microscopy measurements that L.M., T.L., X.B. and Y.Y. performed. J.N. collected the neutron diffraction data. All authors discussed the data and reviewed the final draft.

Competing interests

The authors declare no competing interests.

Additional information

Supplementary information is available for this paper at https://doi.org/10.1038/s41560-018-0309-7.

Reprints and permissions information is available at www.nature.com/reprints.

Correspondence and requests for materials should be addressed to P.A.G. or J.L. or X.J.

Publisher's note: Springer Nature remains neutral with regard to jurisdictional claims in published maps and institutional affiliations.